Deciphering the exceptional kinetics of hierarchical nitrogen-doped carbon electrodes for high-performance vanadium redox flow batteries

Yang Li[a], *Shida Yang*[b], *Yunhe Zhao*[a], *Nauman Mubarak*[a], *Mengyang Xu*[c], *Muhammad Ihsan-Ul-Haq*[a], *Tianshou Zhao*[a], *Qing Chen*[a,b*], *Jang-Kyo Kim*[a*]

[a]Department of Mechanical and Aerospace Engineering, The Hong Kong University of Science and Technology, Clear Water Bay, Hong Kong, P. R. China

[b]Department of Chemistry, The Hong Kong University of Science and Technology
Hong Kong, P. R. China

[c]Department of Chemical and Biological Engineering, The Hong Kong University of Science and Technology, Hong Kong, P. R. China

* Corresponding author information:
E-mail: chenqing@ust.hk (Qing Chen)
Email: mejkkim@ust.hk (Jang-Kyo Kim)

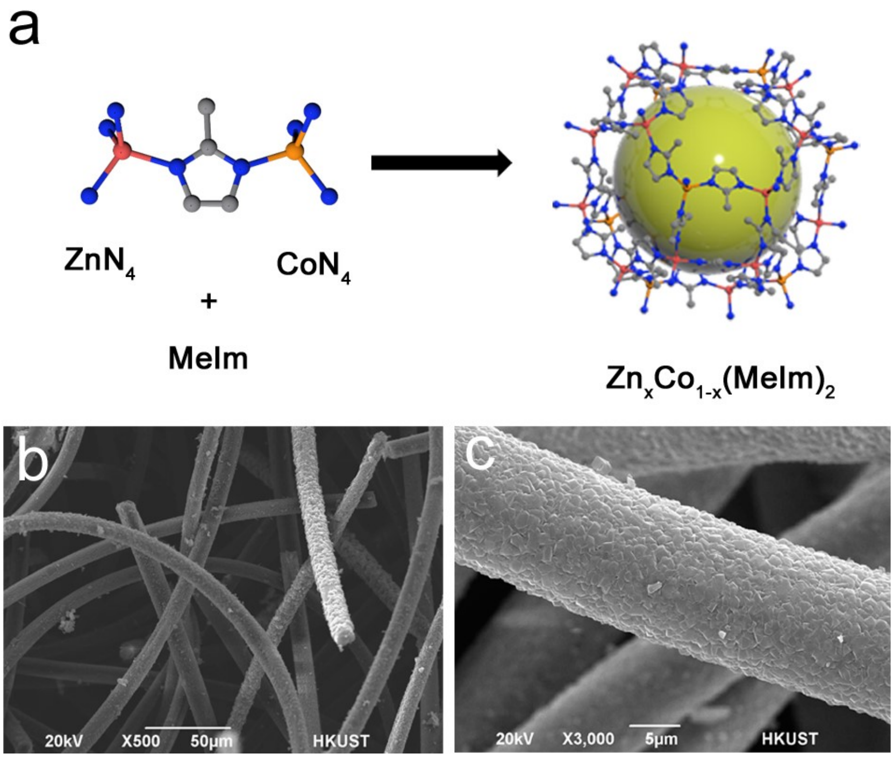

Fig. S1 (a) Schematic illustration of the unit of ZnCo-MOF. (b-c) SEM images of ZnCo-MOF precursor.

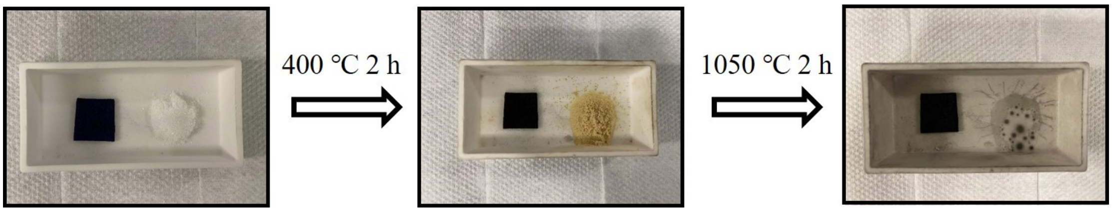

Fig. S2 Evolution of precursor during annealing process.

The evolution of precursors during the annealing process is shown in Fig. S2. At 400 ℃, dicyandiamide undergoes the polycondensation reaction to form carbon nitrides. This pre-stabilized process can avoid its rapid loss (evaporation) at high-temperature pyrolysis. Afterward, ZnCo MOF is carbonized at elevating temperature and the carbon nitrides are also gradually decomposed to small molecular gases (e.g., H_2, NH_3), which can diffuse into the MOF side and facilitate the growth of carbon nanotubes. Finally, there is no residual in the side originally being put dicyandiamide.

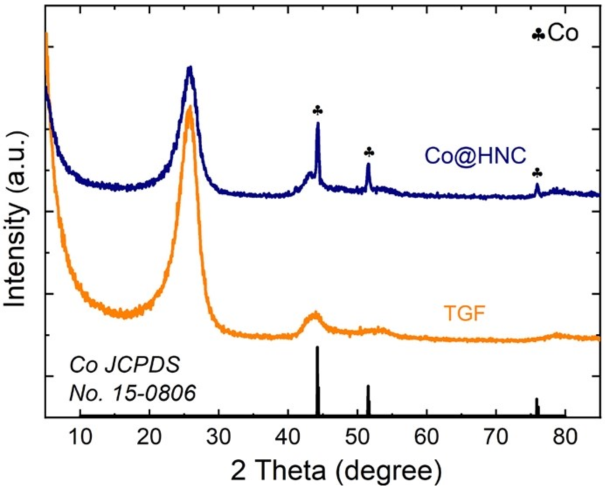

Fig. S3 XRD patterns of thermally treated GF (TGF) and annealed Co@HNC.

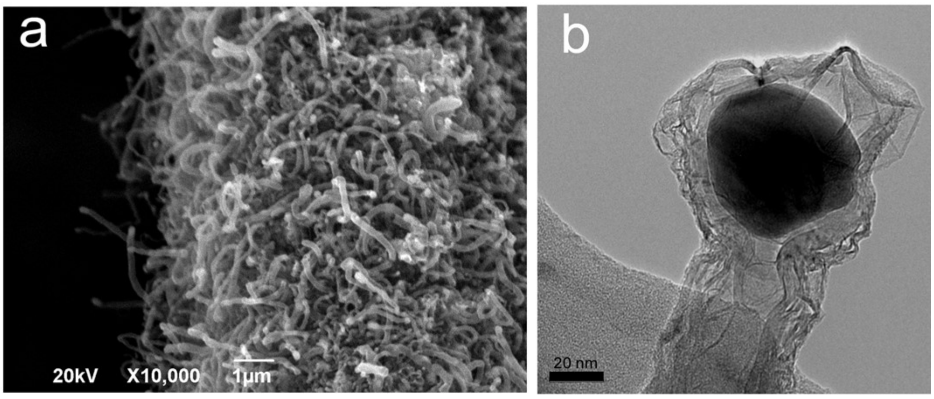

Fig. S4 (a) SEM and (b) TEM images of Co@HNC before acid etching.

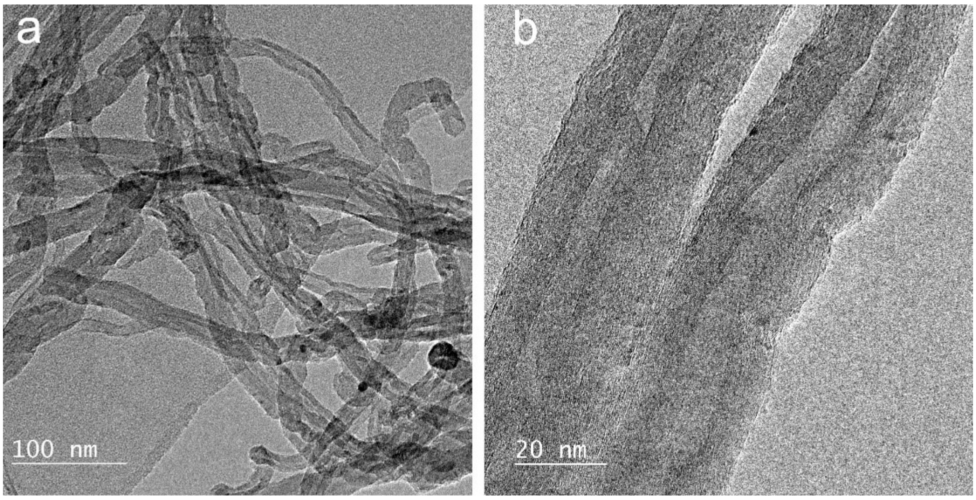

Fig. S5 High resolution TEM images of acid-treated commercial CNTs.

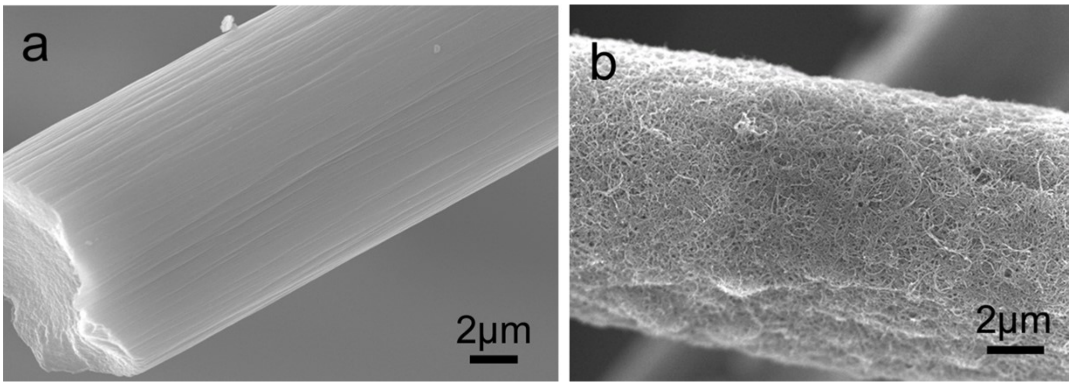

Fig. S6 SEM image of (a) neat TGF and (b) acid-treated commercial CNT coating on TGF (C-TGF).

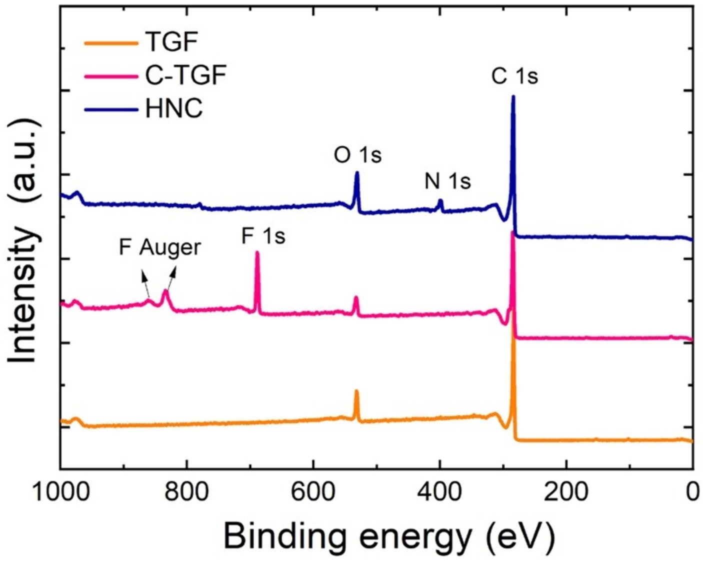

Fig. S7 XPS survey spectra of different electrodes. (Note: the signals of fluorine in C-TGF arises from the Nafion binder.)

Table S1 Elemental compositions of different electrodes measured by XPS.

Electrodes	C (at %)	O (at %)	N (at %)
TGF	91.39	8.39	0.22
C-TGF	92.73	7.27	0
HNC	85.10	9.22	5.68

Fig. S8 Testing device used for diffusion-less CV.

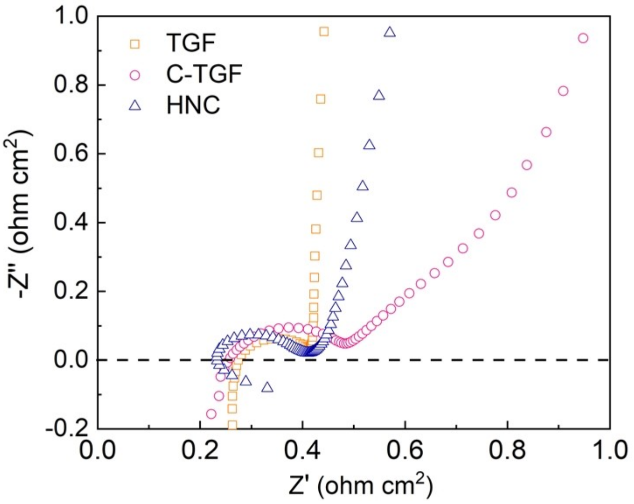

Fig. S9 High-frequency EIS in static cell measured for diffusion-less CV.

The intersection point of curve and X axis (X=0) is the uncompensated resistance in the static cell, which is equal to the sum of electronic resistance and ionic resistance.

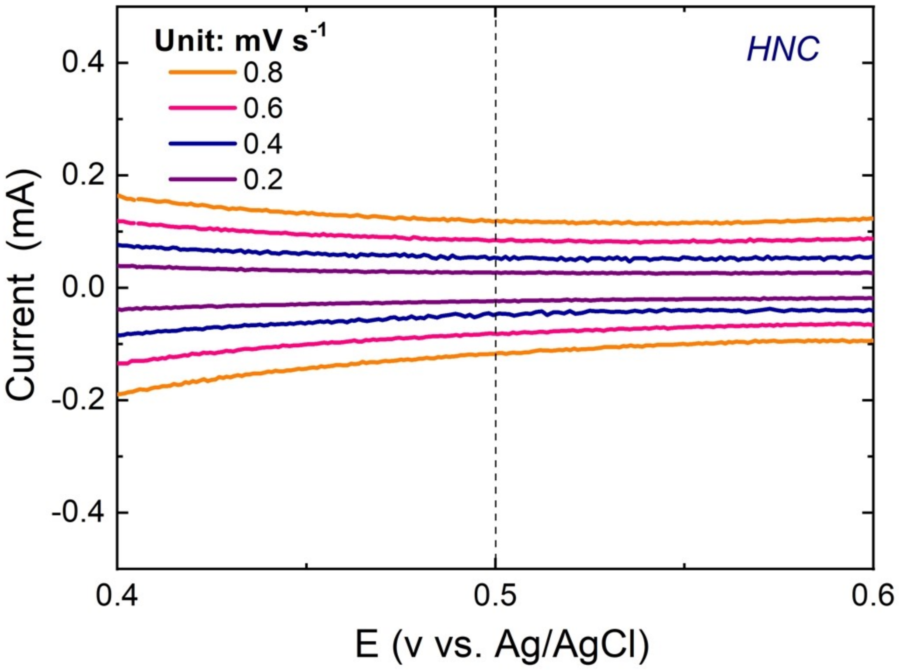

Fig. S10 The diffusion-less CV of HNC in the region of non-Faradaic current at different scan rates.

The double layer capacitance (C_{dl}) can be attained via $C_{dl} = \frac{\Delta j}{v}$, where Δj is the average of the magnitudes of the currents in the forward and backward scans. Assuming a specific capacitance (C_s) for carbon ~20 μF/cm^2, ECSA is then C_{dl}/C_s.

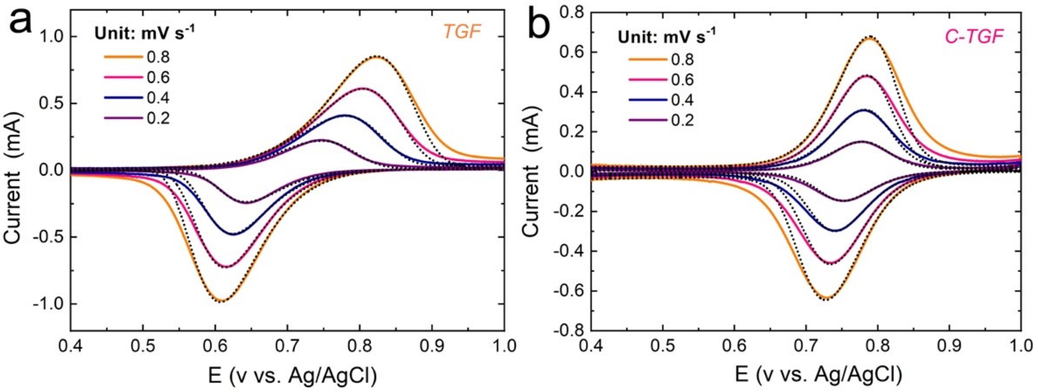

Fig. S11 Diffusion-less CV curves and their simulation results on (a) TGF and (b) C-TGF electrodes.

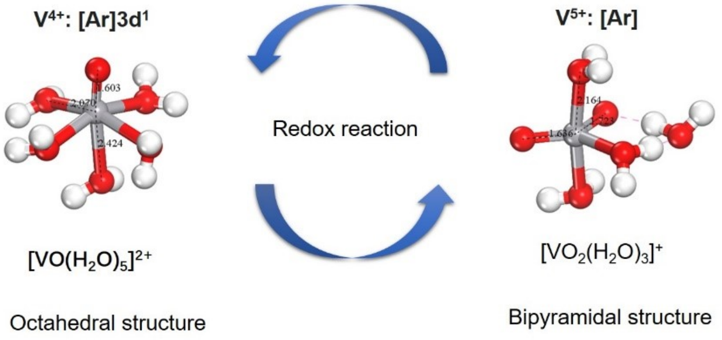

Fig. S12 Optimized solvation structures of vanadium ions

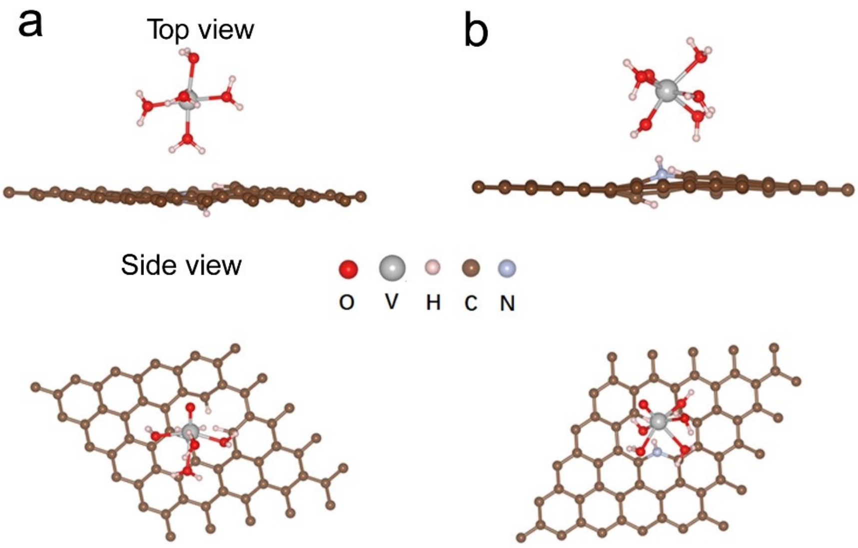

Fig. S13 (a) Initial adsorption models of axial water site on pyridinic-N doped graphene and (b) corresponding optimized model.

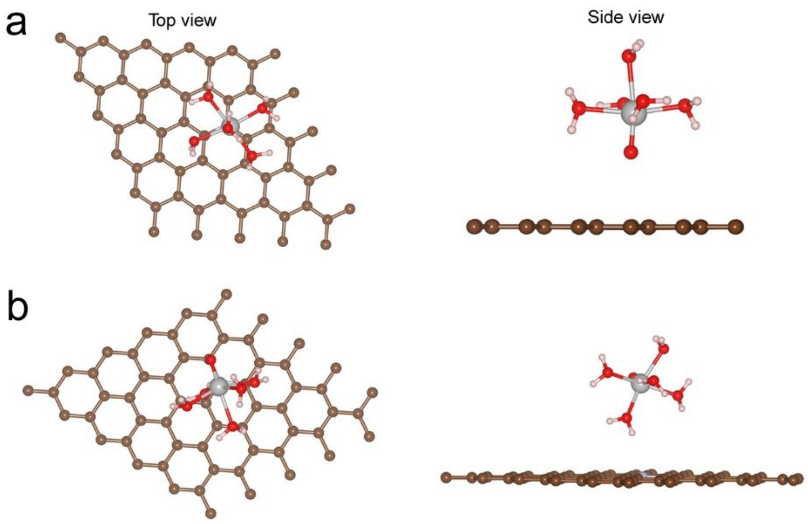

Fig. S14 Optimized models of (a) axial oxygen site and (b) axial water site on graphitic-N doped graphene.

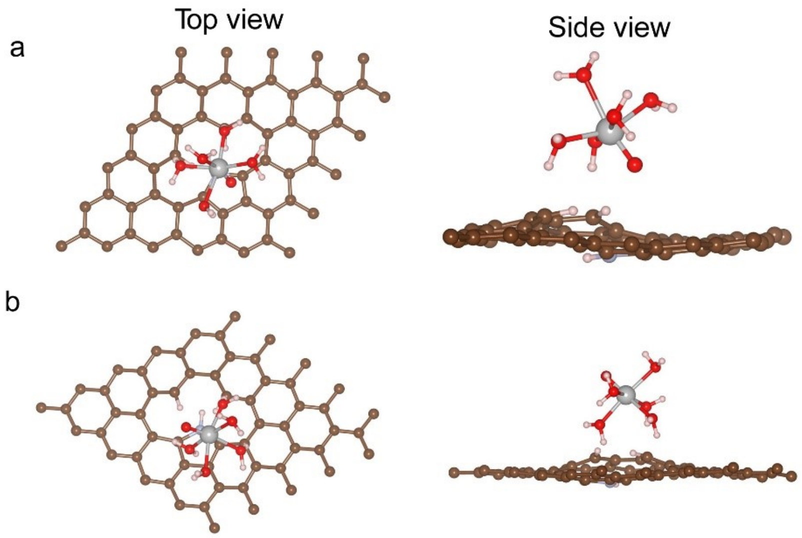

Fig. S15 Optimized models of (a) axial oxygen site and (b) axial water site on pyrrolic-N doped graphene.

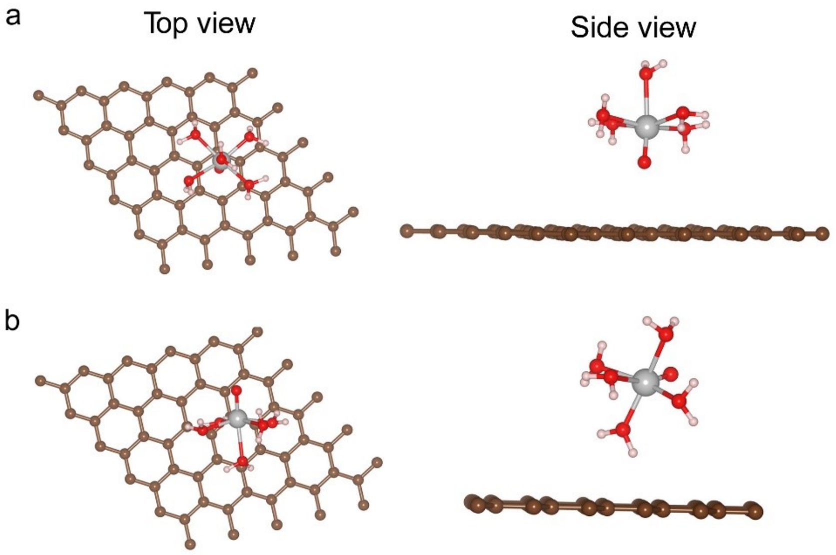

Fig. S16 Optimized models of (a) axial oxygen site and (b) axial water site on pristine graphene.

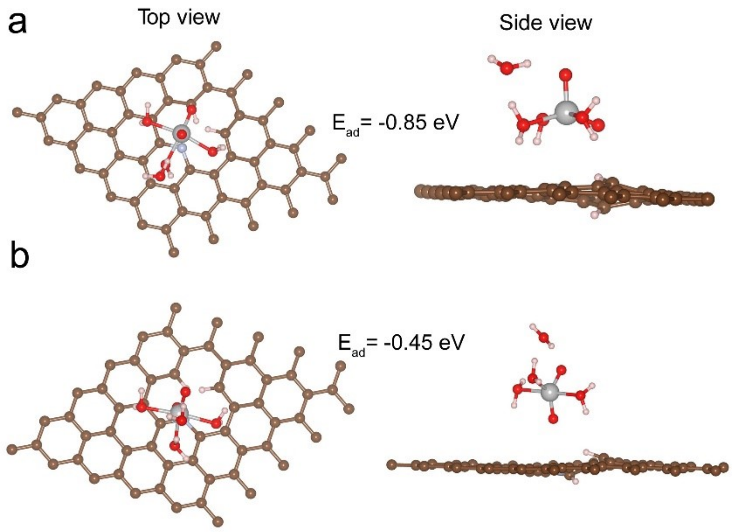

Fig. S17 Optimized models of VO_2^+ on pyridinic-N doped graphene: (a) vanadium site and (b) oxygen site.

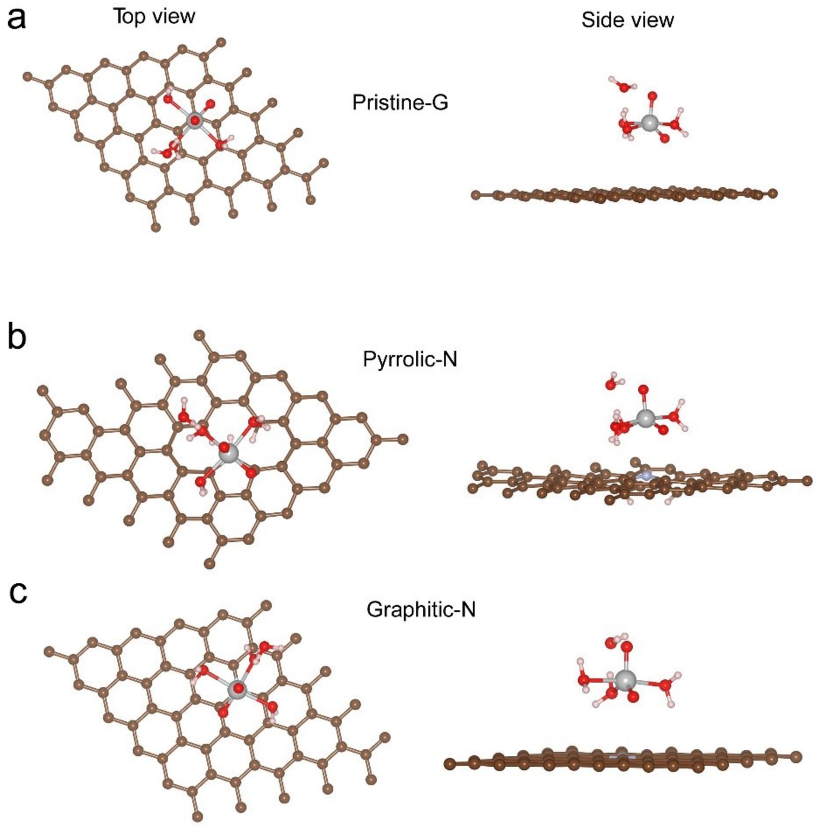

Fig. S18 Optimized models of VO_2^+ on (a) pristine graphene, (b) pyrrolic-N and (c) graphitic-N doped graphene

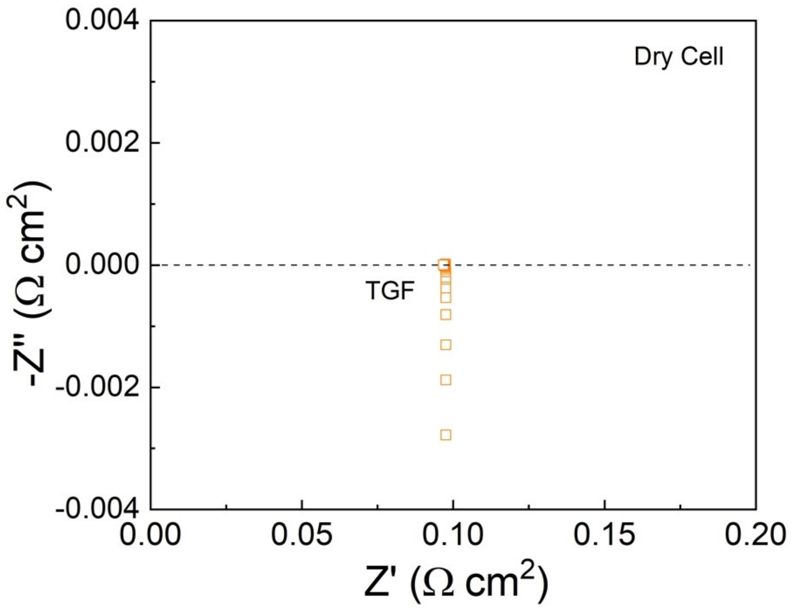

Fig. S19 High-frequency EIS configured with both TGF electrodes in the dry cell

The intersection point of curve and X axis (X=0) is the areal specific resistance in the dry cell, whose value is the sum of the electronic resistances of the carbon electrodes, the endplates and the current leads, and their contact resistances.

Table S2 Electrical conductivity of electrodes.

Electrodes	Electrical conductivity ($S\ cm^{-1}$)
TGF	2.38
C-TGF	3.47
HNC	4.62

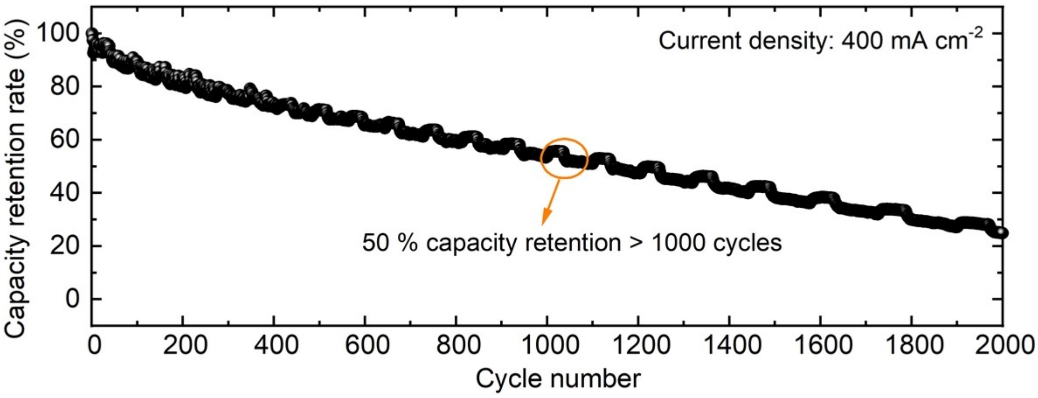

Fig. S20 Capacity retention rate as a function of cycle.

Table S3. Comparison of battery performance between the current study and state-of-the-art VRFBs assembled with different carbon electrodes.

Samples	**Current density (mA cm^{-2})**	**Energy efficiency (%)**	**Cycle number**	**50 % capacity retention (cycles)**	**Reference**
HNC	400	76.8	2000	1032	This work
PCP	400	69.7	700	550	[1]
Gradient GO-rGO/GF	50	87	50	-	[2]
GFs-GO	100	87	100	-	[3]
$KMnO_4$-GF	200	84	550	-	[4]
B_4C-GF	160	80	200	-	[5]
B-doped GF	240	82.5	2000	-	[6]
BiNP-TCC	320	80.1	200	-	[7]
CF-G-1	25	90	100	~90	[8]
N-GF180	100	85	200	-	[9]
CNF-AECF	200	87	500	~460	[10]
Gradient-pore GF	300	68.72	60	-	[11]
P-doped GF	300	75	100	-	[12]
Mxene-GF	200	81.3	500	~480	[13]
MPNCF	320	81.9	500	~490	[14]
Bi-NS-CF	400	80.4	1000	-	[15]
G/CF	100	86.4	660	~590	[16]

Note: For fair comparison batteries are chosen among those with a Nafion®212 membrane.

Reference

1. Y. Li, L. Ma, Z. Yi, Y. Zhao, J. Mao, S. Yang, W. Ruan, D. Xiao, N. Mubarak, J. Wu, T.-S. Zhao, Q. Chen and J.-K. Kim, *J. Mater. Chem. A*, 2021, **9**, 5648-5656.
2. G. Hu, M. Jing, D.-W. Wang, Z. Sun, C. Xu, W. Ren, H.-M. Cheng, C. Yan, X. Fan and F. Li, *Energy Storage Mater.*, 2018, **13**, 66-71.
3. B. Huang, Y. Liu, M. Xia, J. Qiu and Z. Xie, *Sustain. Energy Fuels*, 2020, **4**, 559-570.
4. H. R. Jiang, W. Shyy, Y. X. Ren, R. H. Zhang and T. S. Zhao, *Appl. Energy*, 2019, **233-234**, 544-553.
5. H. R. Jiang, W. Shyy, M. C. Wu, L. Wei and T. S. Zhao, *J. Power Sources*, 2017, **365**, 34-42.
6. H. R. Jiang, W. Shyy, L. Zeng, R. H. Zhang and T. S. Zhao, *J. Mater. Chem. A*, 2018, **6**, 13244-13253.
7. H. R. Jiang, Y. K. Zeng, M. C. Wu, W. Shyy and T. S. Zhao, *Appl. Energy*, 2019, **240**, 226-235.
8. W. Li, Z. Zhang, Y. Tang, H. Bian, T. W. Ng, W. Zhang and C. S. Lee, *Adv. Sci.*, 2016, **3**, 1500276.
9. Z. He, X. Zhou, Y. Zhang, F. Jiang and Q. Yu, *J. Electrochem. Soc.*, 2019, **166**, A2336-A2340.
10. J. Sun, H. R. Jiang, M. C. Wu, X. Z. Fan, C. Y. H. Chao and T. S. Zhao, *Appl. Energy*, 2020, **271**, 115235.
11. R. Wang, Y. Li and Y.-L. He, *J. Mater. Chem. A*, 2019, **7**, 10962-10970.
12. R. Wang, Y. Li, Y. Wang and Z. Fang, *Appl. Energy*, 2020, **261**, 114369.
13. L. Wei, C. Xiong, H. R. Jiang, X. Z. Fan and T. S. Zhao, *Energy Storage Mater.*, 2020, **25**, 885-892.
14. Q. Wu, X. Zhang, Y. Lv, L. Lin, Y. Liu and X. Zhou, *J. Mater. Chem. A*, 2018, **6**, 20347-20355.
15. X. Zhou, X. Zhang, L. Mo, X. Zhou and Q. Wu, *Small*, 2020, **16**, 1907333.
16. T. Long, Y. Long, M. Ding, Z. Xu, J. Xu, Y. Zhang, M. Bai, Q. Sun, G. Chen and C. Jia, *Nano Res.*, 2021, **14**, 3538-3544.